Rhythmic growth of Pacific ferromanganese nodules and their Milankovitch climatic origin

Xiqiu Han [a,b,*], Xianglong Jin [a,b], Shufeng Yang [c], Jan Fietzke [d],
Anton Eisenhauer [d]

[a] *Key Laboratory of Submarine Geosciences, State Oceanic Administration, Hangzhou 310012, PR China*
[b] *Second Institute of Oceanography, State Oceanic Administration, Hangzhou 310012, PR China*
[c] *Department of Earth Sciences, Zhejiang University, Hangzhou 310027, PR China*
[d] *GEOMAR Research Center for Marine Geosciences, Wischhofstrasse 1–3, D-24148 Kiel, Germany*

Abstract

The internal microstructure of a ferromanganese nodule (#2392, from 154°37.52′W, 9°37.56′N, at water depth 5194 m) was examined in detail on polished sections, and radiometrically dated ($^{230}Th_{ex}/^{232}Th$) along a high-resolution (0.1 mm) depth profile (0–1.3 mm), spanning approximately 271 ka. The fabric shows typical stromatolithic structure and exhibits four orders of basic cyclic growth pattern, namely laminae bands, laminae zones, laminae groups and laminae pairs having average thicknesses of 402–454, 185–206, 58–67 and 15–18 μm, respectively. A profile from the depth of 200–2661 μm was selected to obtain the geochemical series using line-scanning electron microprobe analyses, which provide a record of paleoceanographic oscillations during the growth period. Power spectral analysis of the geochemical series for Al, Mn, Fe and Fe/Mn from the depth of 200–1220 μm, where no obvious discontinuity could be observed, display conspicuous cyclicities. The cycles of laminae zones, laminae groups and laminae pairs are reflected in the spectral patterns as well. The significant spectral peaks are located at 186, 108, 66 μm. Together with the cycle of laminae bands, the ratios of these cyclicities are close to those of Milankovitch orbital cycles. Through tuning to orbital cycles, a net growth rate of 4.5 mm/Ma is derived for the profile, which is in perfect agreement with the growth rate of 4.6 mm/Ma determined by $^{230}Th_{ex}/^{232}Th$ dating. Therefore, the rhythmic growth of ferromanganese nodules appears definitely associated with Milankovitch cycles, and the growth cyclicities may offer a new tool for estimating growth rates of ferromanganese nodules and paleoenvironmental reconstruction at substage resolution when supported by radiometric dating.
© 2003 Elsevier Science B.V. All rights reserved.

Keywords: Rhythmic growth; Milankovitch cycles; $^{230}Th_{ex}/^{232}Th$ dating; growth rate; Ferromanganese nodules; Pacific Ocean

* Corresponding author.
E-mail addresses: xqhan@mail.hz.zj.cn (X. Han),
xljin@mail.hz.zj.cn (X. Jin), yjsy-ysf@sun.zju.edu.cn
(S. Yang), jf@gpi.uni-kiel.de (J. Fietzke),
aeisenhauer@geomar.de (A. Eisenhauer).

1. Introduction

The most prominent feature of ferromanganese nodules is their concentric layering and internal stromatolithic laminar growth rhythm (Fig. 1). Although their growth structure and origin have

been discussed in numerous publications [1–8], few general mechanisms linking the variety of laminar rhythms to growth or environmental conditions have been proposed. Considering the inherent cyclic nature of the lamination in many ancient stromatolites has led to several attempts to interpret particular cyclic sequences in terms of their contemporary periodicities, such as days, months and years, and hence to infer values for the past rates of the Earth's rotation [9–11]. Therefore, it is intriguing to examine more closely the cyclic information recorded by the deep-sea ferromanganese nodules. Since the thickness of one individual lamina of Pacific hydrogenetic manganese nodules is commonly on the order of several microns, and since it is well accepted that their growth rates are on the order of 1–10 mm/Ma [2,12–15], we will test the idea of whether or not the rhythmic growth of manganese nodules is an orbital-related phenomenon based on micro-textural and geochemical analysis as well as high-resolution radioisotope dating.

There is a general problem in dating deep-sea ferromanganese nodules with high resolution. The most precise dating methods are ^{230}Th and ^{10}Be [13–17], however, pelagic ferromanganese nodules grow very slowly, and the spatial resolution in analyzing nodules is usually restricted to ∼ 0.1 mm due to the amount of sample material needed for chemical preparation. It has also not been possible to resolve time routinely to better than 0.5–1 Ma [15]. Furthermore, if the age of ferromanganese nodule is older than 10 Ma, there is no available alternative dating method that may be employed because ^{230}Th is applicable for only the past 400 ka, whereas ^{10}Be extends chronologies back to ∼ 10 Ma.

If an orbital imprint exists in the growth record of ferromanganese nodules, the links between the Earth's orbital cycles, climate, and environmental conditions will provide an excellent opportunity to determine their ages to an accuracy of 10–20 ka. Therefore, the main objective of this paper is to examine the possible Earth orbital imprints on the rhythmic growth pattern of a Pacific ferromanganese nodule through tuning the cyclicities of its fine-scale geochemical record revealed by power spectral analysis to Milankovitch cycles

and corroborating these with high-resolution ^{230}Th–^{232}Th dating.

2. Samples and methods

Nodule #2392 was collected in the Clarion–Clipperton fracture zone in the central Pacific Ocean at 154°37.52′W, 9°37.56′N at a water depth of 5194 m during the Dy85-4 Cruise organized by the State Oceanic Administration of China in 1996. The nodule is spheroidal with approximate dimensions of $2.45 \times 2.45 \times 2.0$ cm. The surface is smooth, suggesting a hydrogenetic origin [1,3]. Its associated sediment is siliceous clay.

The nodule was cut into two halves longitudinally and polished. One half was used for both growth pattern studies using reflected-light microscope and in situ microprobe analysis, the other half was used for high-resolution radioisotope dating. Based on the micro-textural observation, a composite growth profile was selected for line-scanning analysis to obtain the variations of X-ray intensities for 12 elements (Al, Fe, Mn, Si, Ca, Mg, Ti, Ba, Cu, Co Ni, P) using the JEOL JXRA-8600 Electron Microprobe at Nanjing University. The acceleration voltage was 15 kV; probe current was 1.013×10^{-8} A; scan steps were 0.5 μm. In addition, 10 points along this profile were selected to conduct point analyses for calibration as well as to get a representative composition of the growth laminae with different reflectivity. The power spectral analysis [19] was used to analyze the geochemical series of Al, Fe, Mn and Fe/Mn to obtain the oscillatory cycles hidden in the data [20]. The X-ray intensity is a function of element concentration [18]. To avoid bringing in errors, we used raw X-ray intensity data for spectral analysis. The significant regular cyclicity in the depth domain can be taken as a regular cycle in the time domain, and when this cycle is known, the net growth rate can be inferred.

For radiometric dating, one continuous depth profile of the uppermost 1.3 mm was sampled at 0.1 mm intervals using a drilling machine with a numerically controlled drive [15]. The nodule was fixed to a sample holder in order to guarantee vertical positioning of the drill bit (3 mm in diam-
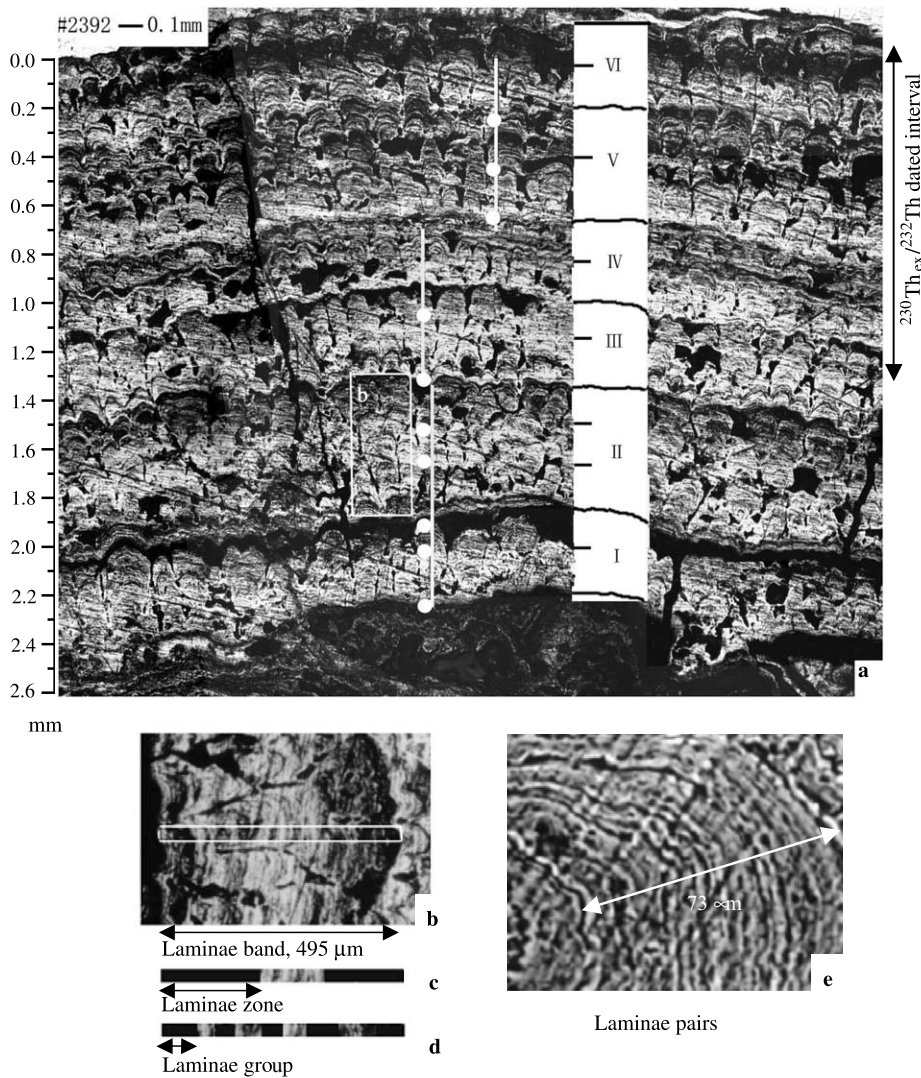
Fig. 1. (a) Micro-texture of outermost coating of Nodule #2392 comprising the uppermost 2660 μm consisting of six laminae bands (see depth scale and boundaries of Bands I–VI; scale bar = 100 μm); stromatolithic columnar growth and cycle hierarchy are evident. White lines are profiles from which the composite geochemical series were obtained using line-scanning analysis with the electron microprobe; dots on the lines indicate point analyses listed in Table 3. Black arrow indicates ^{230}Th/^{232}Th-dated interval. Inset (b): Laminae Band II consists of three laminae zones (b, c), each zone of two to four laminae groups (d); laminae pairs shown in (e).

eter) relative to the surface of the nodule. A total of 13 samples were thus collected yielding between 0.4 and 3 mg of material per sample. Table 1 shows that the first three samples from the depth of 0–0.3 mm have relatively low weights, this is because the drilled areas were smaller for the top

part of the nodule where the surface is slightly curved, and where the drill bit did not fully penetrate. Complete sampling first occurred at depths below 0.3 mm.

The drilled samples were weighed and placed into Teflon beakers containing 200 μl of ^{229}Th

spike (102.9 ± 0.2 pg/g) and 300 μl of ^{236}U spike (239.9 ± 0.1 pg/g). About 8 ml 7 N HNO_3 and 100 μl H_2O_2 were added to the samples. This solution was evaporated to dryness at 130°C. After addition of 8 ml 7 N HNO_3 the samples were ready for ion chromatographic separation.

Bio-Rad 10 ml polypropylene columns were loaded with 2 ml Bio-Rad 1×8 resin. The resin and column were cleaned twice (20 ml 7 N HNO_3, 20 ml 7 N HCl, 20 ml H_2O) and preconditioned with 20 ml 7 N HNO_3. The dissolved samples were loaded onto the column. After cleaning with 20 ml 7 N HNO_3 the thorium fraction was eluted by 10 ml 7 N HCl into a Teflon beaker. To dissolve residual resin 50 μl $HClO_4$ were added. The solution was evaporated to dryness at 160°C. After addition of 3 ml 5% HCl the thorium samples were ready for inductivity-coupled-mass spectrometry (ICP-MS) analysis. The uranium fraction was eluted by 10 ml H_2O ultrapure water (18.2 MOhm), suprapure $HClO_4$ and H_2O_2; subboiled distilled HCl and HNO_3 were used for all chemical treatments. The total procedural blank amounts are 2.7 ± 1.5 fg for ^{230}Th, 50.49 ± 4.78 pg for ^{232}Th, 5.9 ± 1.7 fg for ^{234}U and 945 ± 22 fg for ^{235}U.

The measurements of $^{234}U/^{236}U$, $^{235}U/^{236}U$ and $^{230}Th/^{229}Th$ were carried out with the Micromass PlasmaTrace2 (PT2)-high-resolution (HR)-ICP-MS at the Geological Sciences Institute at Kiel University, equipped with a Cetac MCN 6000 desolvator and a self-aspiring microconcentric glass nebulizer ('MicroMist' 100 μl). Further measurements ($^{232}Th/^{229}Th$) were performed at the GEOMAR Research Center, on an AXIOM Multicollector (MC)-ICP-MS equipped with a Cetac Aridus. The ratio $^{232}Th/^{229}Th$ was determined using the MC-ICP-MS because of its wide dynamic range. The background for each isotope ratio was estimated prior to the measurements of the sample. The sensitivity was determined using a 100 ppt ^{238}U solution. Typical sensitivities are higher than about 25 GHz/ppm for the PT2 in 400 Res mode, > 15 GHz/ppm for the PT2 in 800 Res mode, and > 20 GHz/ppm for the AXIOM in 400 Res mode, respectively.

3. Results

3.1. The characteristics of rhythmic growth and cycle hierarchy

The ferromanganese Nodule #2392 has a core

Table 1
$^{234}U/^{238}U$ and $^{230}Th_{ex}/^{232}Th$ ratios, $^{234}U/^{238}U$ ages and $^{230}Th_{ex}/^{232}Th$ ages from the high-resolution profile of the uppermost 1.3 mm of Nodule #2392

Depth interval (mm)	Weight (mg)	^{238}U (ppm)	$^{234}U/^{238}U$ activity ratio (‰)	$^{230}Th_{ex}$ (ng/g)	^{232}Th (ppm)	$^{230}Th_{ex}/^{232}Th$	Error	$^{230}Th_{ex}/^{232}Th$ age (ka)
0.0–0.1	0.448	2.182 ± 0.006	143 ± 8.5	6.57 ± 0.01	$13\,917 \pm 8.5$	4.721E-04	2E-06	0–22
0.1–0.2	0.757	2.466 ± 0.005	154 ± 5.5	6.94 ± 0.005	$14\,562 \pm 17$	4.763E-04	1E-06	22–43
0.2–0.3	1.435	2.824 ± 0.005	131 ± 3.5	7.08 ± 0.01	$15\,627 \pm 13$	4.529E-04	1E-06	43–65
0.3–0.4	2.122	3.250 ± 0.003	144 ± 3.0	7.04 ± 0.005	$17\,193 \pm 13.5$	4.095E-04	8E-07	65–87
0.4–0.5	2.023	3.757 ± 0.005	133 ± 3.0	7.18 ± 0.01	$19\,280 \pm 13.5$	3.724E-04	1E-06	87–108
0.5–0.6	2.325	4.279 ± 0.003	136 ± 2.5	7.16 ± 0.01	$22\,390 \pm 20$	3.196E-04	1E-06	108–130
0.6–0.7	2.189	4.920 ± 0.004	132 ± 2.5	6.75 ± 0.01	$27\,324 \pm 26$	2.472E-04	8E-07	130–152
0.7–0.8	1.641	5.303 ± 0.003	125 ± 2.5	6.07 ± 0.005	$29\,681 \pm 31.5$	2.045E-04	6E-07	152–174
0.8–0.9	2.923	5.497 ± 0.008	118 ± 2.0	5.16 ± 0.005	$30\,853 \pm 25$	1.673E-04	5E-07	174–195
0.9–1.0	2.927	5.534 ± 0.006	102 ± 1.5	4.38 ± 0.005	$31\,857 \pm 27$	1.375E-04	4E-07	195–217
1.0–1.1	3.192	5.667 ± 0.007	110 ± 2.0	3.34 ± 0.005	$31\,060 \pm 27$	1.076E-04	3E-07	217–239
1.1–1.2	3.124	6.059 ± 0.003	98 ± 1.5	2.78 ± 0.005	$31\,899 \pm 31$	8.727E-05	3E-07	239–260
1.2–1.3	3.632	6.356 ± 0.005	87 ± 2.0	2.02 ± 0.005	$33\,742 \pm 28.5$	6.000E-05	2E-07	260–282

The $^{234}U/^{238}U$ activity ratio is presented as deviation in permil (‰) from the equilibrium value. The excess ^{230}Th ($^{230}Th_{ex}$) was calculated by subtracting the amount of ^{230}Th in secular radioactive equilibrium with the measured ^{238}U concentrations from the originally measured ^{230}Th concentration.

and outer coatings. The coatings display typical concentric layers, which can be identified easily by the unaided eye. There are mechanically deposited sediments between the coatings, which represent discontinuities in the growth sequence. Under a reflected-light microscope, it is noted that each coating always shows typical stromatolithic structures consisting of locally coalescing columnar and branching features, mostly subcylindrical in shape and having a diameter of 0.04–0.1 mm and a height ranging from 0.38 to 0.5 mm (Fig. 1a). The small openings between the columns are usually filled with inorganic and biogenic detrital sediments. Each column is composed of very fine laminae (Fig. 1a,e). They are gently domed or flat and can be correlated and traced to corresponding positions of different columns, which seem to represent periods of uniform growth (Fig. 1a). The mineral components of hydrogenetic manganese nodules are mainly an intimate mixture of δ-MnO_2, X-ray amorphous $FeOOH \cdot nH_2O$ and small portions of aluminosilicate [18,21].

Visual changes in growth pattern and reflectance allow distinguishing four different scales of cyclicity in the outer coating of Nodule #2392: laminae bands, laminae zones, laminae groups and laminae pairs (see Fig. 1). This phenomenon is commonly observed in deep-sea hydrogenetic manganese nodules [18]. Fig. 1a shows that the outermost coating of Nodule #2392 contains six laminae bands (the first order). The bands usually start from a horizontal or wavy structure and then change into a columnar structure. It seems that the stromatolithic columns in Bands I–IV are more compact than those in Bands V and VI.

Two distinct reflectivity variations can be recognized within each band, except for Band III, where three variations can be recognized (Fig. 1a–c). Usually the lower part of the band contains some clay and appears darker in reflectivity, followed by a brighter part. We defined these variations as laminae zones (the second order). There are 13 laminae zones altogether shown in Fig. 1a. Each laminae zone contains two to four laminae groups (the third order), which are separated by several relatively dark laminae (Fig. 1a–d). Each laminae group consists of five to six laminae pairs (the fourth order), and every laminae pair comprises a very fine dark lamina followed by a lighter colored one (Fig. 1e). The average thicknesses for the laminae bands, laminae zones, laminae groups, and laminae pairs are about 402–454, 185–206, 58–67 and 15–18 μm, respectively (Table 2). Clearly, the different scales of superimposed cycles in the growth profile of the nodule display a well-developed hierarchy.

3.2. Geochemical series

As nodules grow in layers around a core, their chemical compositions may record the chronological information of the environmental parameters of formation. Mn, Fe, Si and Al are the major elements of ferromanganese nodules (Table 3). Among them, Mn and part of the Fe mainly exist in the form of δ-MnO_2 and X-ray amorphous $FeOOH \cdot nH_2O$, respectively. Al, part of Si, and a smaller fraction of the Fe are bound mainly in the mechanically deposited aluminosilicates. The other part of Si comes from siliceous organisms, for

Table 2
Thicknesses of laminae bands, laminae zones, laminae groups, and laminae pairs in the outermost coating of Nodule #2392

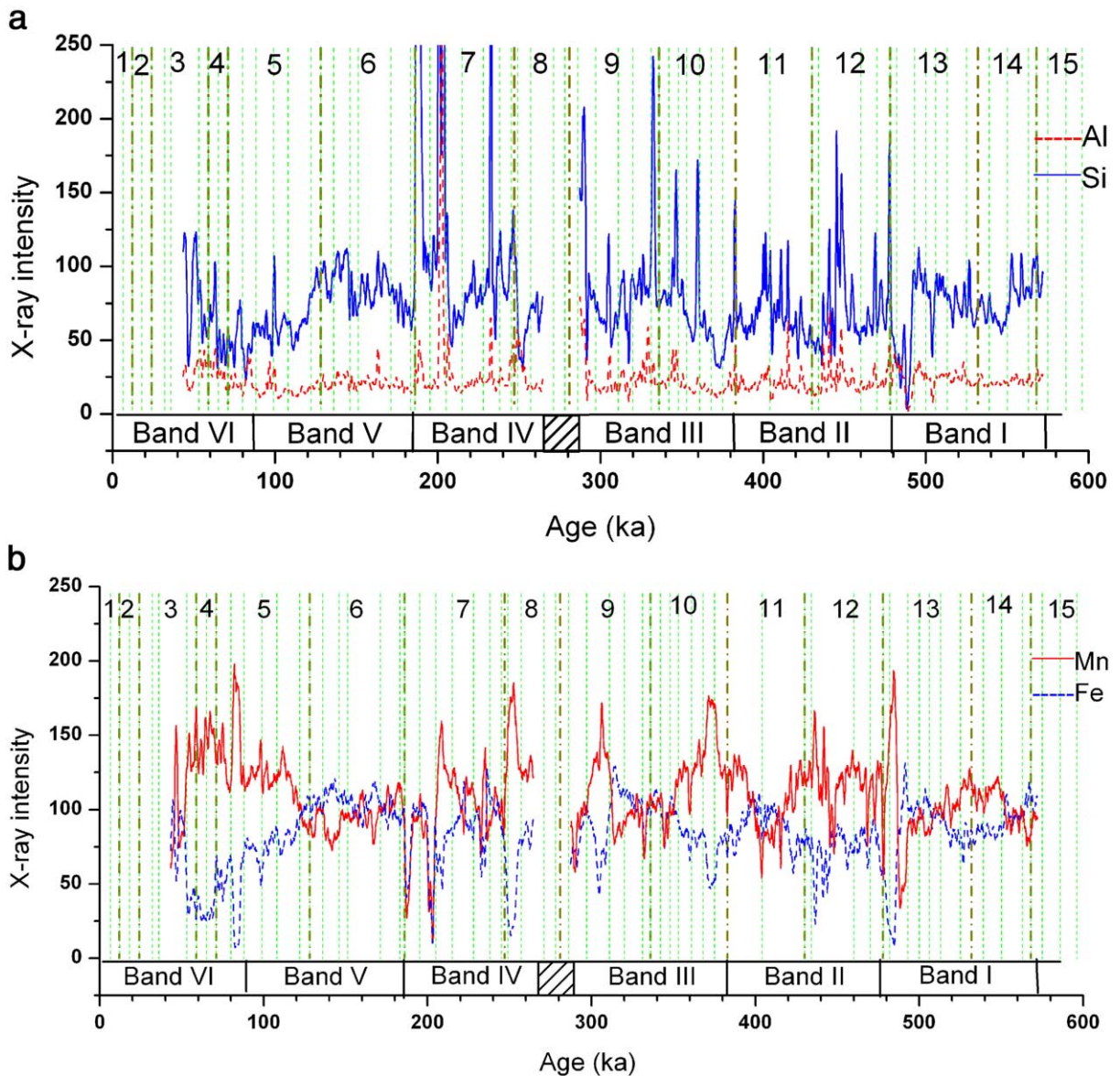| Laminae band no.	Thickness of laminae bands (μm)	Thickness of laminae zones (μm)	Thickness of laminae groups (μm)	Thickness of laminae pairs (μm)
Band VI	350–418	175–209	58–68	15–18
Band V	428–450	214–225	61–71	15–19
Band IV	324–361	162–180	51–59	14–15
Band III	362–403	181–201	59–65	15–17
Band II	562–600	187–200	60–64	15–17
Band I	380–440	190–220	60–73	15–20
Average	402–454	185–206	58–67	15–18

Fig. 2. High-resolution elemental profiles obtained by line-scanning electron microprobe analysis from the outermost coating of Nodule #2392. The depth resolution is 0.5 μm, raw data have been smoothed by a 10-point moving average. The time scale of the uppermost 1.3 mm (Bands VI–IV) is according to $^{230}Th_{ex}/^{232}Th$ dating. From the depth of 1.3–2.6 mm (Bands III–I) the age is estimated based on the orbital imprint and that every laminae band corresponds to the short eccentricity cycle of 95 ka. The laminae band boundaries of the profile are located as follows: Band VI: 0–417 μm (0–91 ka), Band V: 417–858 μm (91–186 ka), Band IV: 858–1219 μm (186–264 ka), Band III: 1219–1622 μm (287–382 ka), Band II: 1622–2221 μm (382–477 ka), Band I: 2221–2661 μm (477–572 ka), The hiatus between Bands IV and III is 22 ka derived from $^{230}Th_{ex}/^{232}Th$ dating. The time resolutions are 22 ka. Oxygen isotope stages and substages are based on the SPECMAP marine oxygen isotope stack [27,29,30]. The ages of the stage boundaries adopted here are: 1/2: 12 ka, 2/3: 24 ka, 3/4: 59 ka, 4/5: 71 ka, 5/6: 128 ka, 6/7: 186 ka, 7/8: 247 ka, 8/9: 281 ka, 9/10: 336 ka, 10/11: 383 ka, 11/12: 430 ka, 12/13: 478 ka, 13/14: 532 ka, 14/15: 568 ka. (a) Si, Al; (b) Fe, Mn.
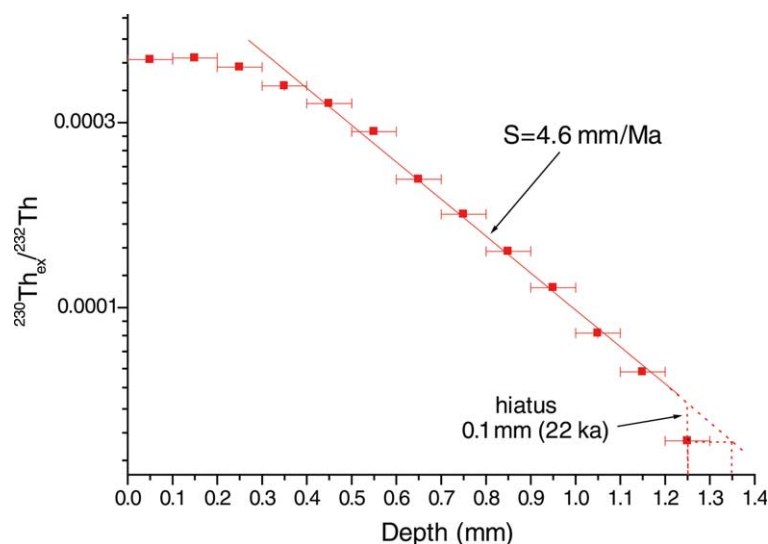
Fig. 3. $^{230}Th_{ex}/^{232}Th$ activity profile of Nodule #2392 (Depth: 0–1.3 mm, see Fig. 1). The first three points were omitted from the regression because of sampling artifacts (see text). The last data point was also omitted because of a hiatus between Bands III and IV. The resulting fit of the remaining data points indicates a growth rate of 4.6 mm/Ma; the duration of the hiatus is 22 ka.

example, diatoms or radiolarians. Fig. 2 shows the X-ray intensities for Si, Al, Fe and Mn of the outermost coating of Nodule #2392 obtained by line-scanning electron microprobe. Fe is strongly inversely correlated with Mn, while Al and Si are usually but not always correlated to each other, since the source of Si could be from both aluminosilicates and siliceous organism. The variation in the contents of Fe, Mn and Al is believed to be associated with the supply of Fe, Mn, and detrital sediment from the water column, which in turn is strongly related to environmental conditions and climatic oscillations during the nodule's growth history [15,22–23].

3.3. Age and growth rates

The results of the isotope measurements are presented in Table 1, Figs. 3 and 4. Both the $^{230}Th_{ex}/^{232}Th$ and the $^{234}U/^{238}U$ ratios decrease

Table 3
Chemical composition of samples analyzed by electron microprobe (weight %)

| Position	SiO$_2$	Al$_2$O$_3$	FeO	MnO	CaO	MgO	TiO$_2$	P$_2$O$_5$	CuO	BaO	CoO	NiO
1 (D)	14.50	2.94	34.32	22.77	2.91	1.36	2.74	0.89	0.16	0.30	0.34	0.10
2 (D)	12.29	3.31	29.90	23.61	2.81	1.52	2.69	0.97	0.01	0.23	0.74	0.17
3 (D)	8.01	2.43	20.93	33.26	4.56	1.08	1.65	1.25	0.16	0.27	0.40	0.51
4 (D)	9.49	2.79	22.65	31.36	3.23	1.23	1.59	0.65	0.36	0.20	0.59	0.40
5 (D)	11.47	2.97	27.44	29.22	3.25	1.49	2.25	0.83	0.26	0.15	0.74	0.27
6 (D)	13.67	4.92	27.99	24.93	2.80	1.18	2.17	0.78	0.23	0.33	0.52	0.24
7 (D)	12.14	2.87	29.32	25.74	2.98	1.28	2.38	0.85	0.28	0.18	0.49	0.22
8 (B)	0.76	5.42	4.20	47.10	1.69	8.64	0.50	0.15	2.12	0.13	0.24	3.13
9 (B)	5.02	3.54	9.19	41.61	2.11	4.00	1.29	0.30	1.42	0.26	0.81	2.39
10 (B)	0.66	3.10	0.98	51.47	2.25	4.87	0.12	0.07	1.71	0.12	0.04	6.30
Ave. (D)	11.65	3.18	27.51	27.27	3.22	1.31	2.21	0.89	0.21	0.24	0.55	0.27
Ave. (B)	2.15	4.02	4.79	46.73	2.02	5.84	0.64	0.17	1.75	0.17	0.36	3.94

D = darker microlayer, B = brighter microlayer.
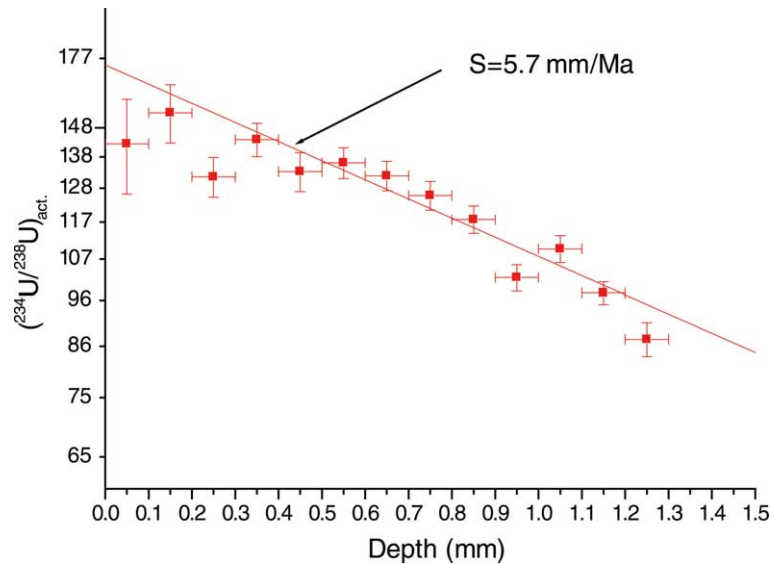
Fig. 4. $^{234}U/^{238}U$ profile of Nodule #2392 (Depth: 0–1.3 mm). The first three points and the last point were omitted from the regression (see text). The slope of a logarithmic fitting of the remaining points indicates a growth rate of 5.7 mm/Ma.

as a function of depth. The $^{230}Th_{ex}/^{232}Th$ profile appears more continuous than the $^{234}U/^{238}U$ profile. Except for the first three data points and the last one, all other data points fall almost exactly on the logarithmic linear fitting lines. The 'flattening' of the $^{230}Th_{ex}/^{232}Th$ ratios at the uppermost depth range of 0–0.3 mm results from the different proportions of younger and older material when sampling the top part of the nodule which has a curved surface. Because the younger layer curves downward through the sampled interval, the contribution of the 'older' material decreases with depth until the drill bit fully enters into the nodule. This causes the misleading appearance that the growth rate of the surface is faster than the interior. The last data point falls significantly off the regression line and marks a hiatus, which is also evident from a growth discontinuity at a depth of around 1.22 mm (between Bands IV and III, seen in Fig. 1a).

Accordingly, the average growth rates of about 4.6 and 5.7 mm/Ma are calculated from the logarithmic fit to the $^{230}Th_{ex}/^{232}Th$ and $^{234}U/^{238}U$ ratios, respectively. However, it has been shown that the ($^{234}U/^{238}U$)-chronometer is less reliable because of the diffusion of modern seawater U

into the nodules [24]. The diffusion effect tends to increase the apparent growth rate calculated from the $^{234}U/^{238}U$ ratios relative to the $^{230}Th_{ex}/^{232}Th$ ratios, as is also the case for our nodule. Thus, following only the $^{230}Th_{ex}/^{232}Th$ dating, the depth interval of 0–1.3 mm corresponds to about 271 ± 11 ka and the depth resolution of about 0.1 mm corresponds to ± 11 ka. The hiatus between Bands III and IV is 0.1 mm which corresponds to 22 ka. The duration of the hiatus is calculated from the offset of the last point from the regression line. The offset amounts to 0.1 mm which is converted to time using the growth rate of 4.6 mm/Ma.

4. Discussion

4.1. The Earth orbital imprints on the growth rhythm of the nodule

4.1.1. Spectral analyses of geochemical series

The microstructure of Nodule #2392 shows discontinuities between the boundaries of Bands I and II and Bands III and IV where the depth is 1.22 and 2.22 mm, respectively (Figs. 1 and 2).
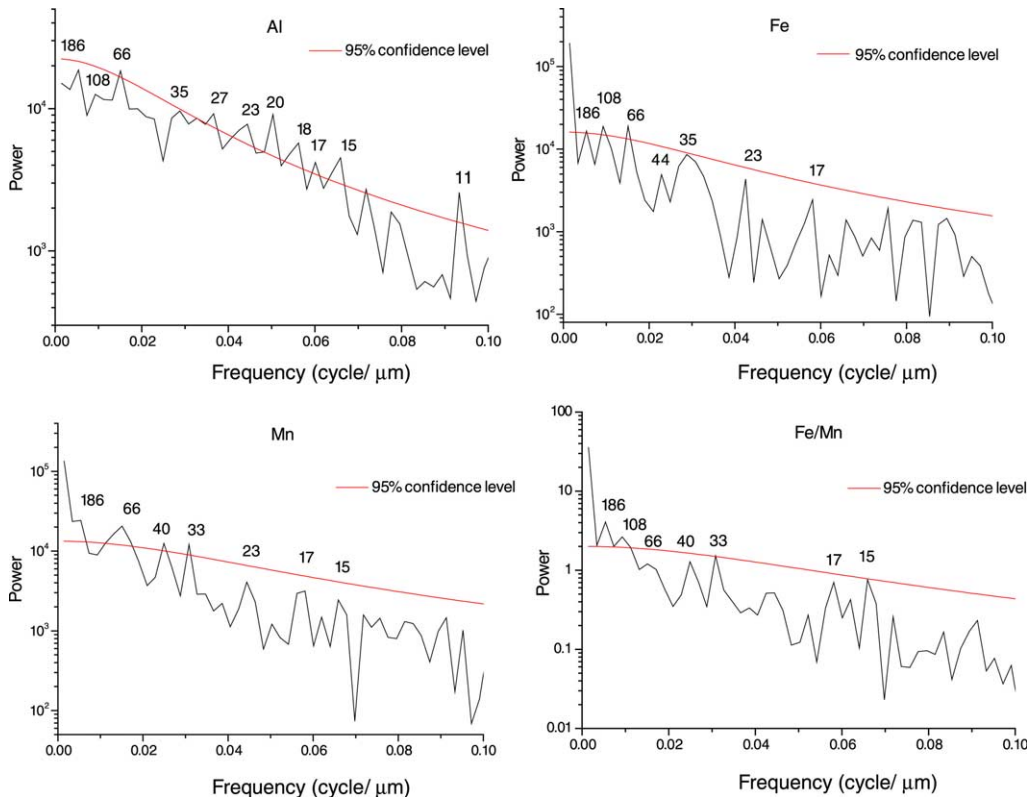
Fig. 5. Power spectral patterns for the Al, Fe, Mn and Fe/Mn series of Nodule #2392 in the depth of 200–1220 μm. Sample interval = 0.5 μm. The periods (wavelength) are expressed as stratigraphic thickness in microns.

Power spectral analysis was carried out for the geochemical series of Al, Fe, and Fe/Mn at a depth of 0.2–1.22 mm (Bands IV–VI), where there is no evident discontinuity, to reveal the periodic oscillation signals hidden in the data. The spectral patterns in the 0.00–0.10 cycles/μm are shown in Fig. 5. The principal peaks of the Al, Fe, Mn and Fe/Mn series occur at 186, 108 (except Mn), 66, 40 and 33–35 μm; there are also several other oscillations at higher frequencies, for example, there are stable peaks at 15, 17 and 23 μm (Fig. 5). The peak of 186 μm is close to the average thickness of a laminae zone, the peak of 66 μm is close to the average thickness of a laminae group, and the peak of 15–23 μm is close to the average thickness of a laminae pair (Table 2, Fig. 5). But restricted by the length of the series, which is only 1020 μm long, the peak which should correspond to the laminae band (402–454 μm) does not ap-

pear. Accordingly, except for the cycle of laminae bands, the other scales of cycles are revealed by the spectral analysis of the geochemical series. The similarity of the spectra strongly implies that there exist regular cycles in time forced by a physical mechanism which affects the growth pattern of deep-sea ferromanganese nodules.

4.1.2. Evidence for Milankovitch cycles in the geochemical series

The motion of the Earth follows various cycles which are related to solar-terrestrial orbital parameters. The main periods of the three most important parameters during the past 5 Ma are eccentricity −100 ka (95 and 123 ka), obliquity −41 and 54 ka and precession −23 and 19 ka [25,26]. Fig. 5 shows that the prominent peaks of the geochemical series from the depth between 200 and 1220 μm are at 186, 108, 66, 40 and 33–35 μm.

Table 4
Observed and postulated periodicities obtained from the power spectral analysis of Al, Fe, Mn and Fe/Mn series for the depth profile of 200–1220 µm of Nodule #2392 compared with present Milankovitch orbital periods, assuming the peak of 186 µm corresponds to the cycle of obliquity

		Orbital parameter		
		Eccentricity	Obliquity	Precession
Al	cycles in space domain (µm)		186	108
	postulated periods in time domain (ka)		41	24
Fe	cycles in space domain (µm)		186	108
	postulated periods in time domain (ka)		41	24
Mn	cycles in space domain (µm)		186	
	postulated periods in time domain (ka)		41	
Fe/Mn	cycles in space domain (µm)		186	108
	postulated periods in time domain (ka)		41	24
Laminae band	average thickness (µm)	407		
	postulated period in time domain (ka)	91		
Present main orbital periods (ka)		100 (95 and 123)	41	23 and 19

The inferred growth rate is 4.5 mm/Ma. The average thickness of laminae bands in this profile would correspond to 91 ka which is close to a short eccentricity period.

Together with the laminae band cycle which is 407 µm on average along this profile from Bands IV–VI (Figs. 1, 2), we find that the spacing of the cycles can be compared and matched to the spectral peaks of the orbital cycles. There are two possible ways of tuning these results: (1) Assuming that the peak of 186 µm corresponds to the cycle of eccentricity, the ratios of the prominent cyclicities in the Mn series are 108:38:23:19, which is close to the ratios of Milankovitch cycles (100:41:23:19). This would imply a net growth rate of 1.73 mm/Ma, and the average growth cycle of a laminae band would correspond to 235 ka. (2) Assuming that the peak of 186 µm corresponds to the cycle of obliquity, the ratios of

the prominent cyclicities in the Fe series are 41:24:15:8; in Fe/Mn series they are 41:24:9:7 (Fig. 5). Among them, the period of 24 ka corresponds to the cycle of precession, the period of 15–7 ka may be related to the second harmonic of the dominant cycle since the main oscillations are not perfectly sinusoidal, or relevant to the half-precession. The growth cycle of the laminae band would correspond to 91 ka which is close to the short eccentricity cycle. The inferred net growth rate for this assumption would be 4.5 mm/Ma, and the relative errors of the postulated periods to the respective present Milankovitch orbital periods of the tuning would be less than 10% (Table 4).

Table 5
Main cyclicities of the geochemical series in the time domain obtained by power spectral analysis; geochemical time series were transformed from the depth profiles following the growth rate of 4.6 mm/Ma obtained from $^{230}Th_{ex}^{/232}Th$ dating; periods are expressed in ka

Al	Fe	Mn	Fe/Mn
41.5 (1.0)	**41.5** (0.9)	**41.5** (1.0)	**41.5** (1.0)
24.0 (0.7)	**24.0** (1.0)		**24.0** (0.6)
14.7 (1.0)	**14.7** (1.0)	14.7 (0.8)	
7.8 (0.5)	9.7 (0.3)	**8.9** (0.5)	8.9 (0.3)
6.1 (0.5)	**7.8** (0.5)	7.2 (0.5)	**7.2** (0.4)
5.0 (0.4)	5.2 (0.2)	5.0 (0.2)	5.0 (0.1)
4.4 (0.5)	4.8 (0.1)	3.8 (0.1)	3.8 (0.2)

Relative strengths of peaks are shown in parentheses, normalized to the highest peak in each spectrum; periods with >95% significance level are shown in bold.

The $^{230}Th_{ex}/^{232}Th$ dating revealed a growth rate for the uppermost 1.3 mm of the nodule of 4.6 mm/Ma, which is very close to the growth rate of 4.5 mm/Ma postulated from the second possibility of the tuning results. Accordingly, it seems very clear that there is an orbital imprint on the growth of the ferromanganese nodule; the growth cycles of laminae bands and zones correspond to the periods of eccentricity and obliquity, respectively.

To further test the hypothesis of an orbital imprint, we transformed the geochemical profiles into time series using the growth rate of 4.6 mm/Ma obtained from $^{230}Th_{ex}/^{232}Th$ ratios. The spectral analysis results of the Al, Fe, Mn and Fe/Mn series in the time domain are shown in Table 5. They reveal that the geochemical time series of the nodule in the past 271 ± 11 ka contains periods of 41.5, 24.0 and 14.7 ka. If we transform the depth profiles into time series with the growth rate of 5.7 mm/Ma as obtained from $^{234}U/^{238}U$ ratios, the periods would be located at 32.0, 18.5 and 11.4 ka, which lack physical significance and are also inconsistent with the tuning results. At this point, we conclude that the radiometric dating could be validated by orbital cycles. The $^{230}Th_{ex}/^{232}Th$ dating results of the nodule are more reasonable or precise than those of $^{234}U/^{238}U$ dating. On the other hand, the growth rates inferred alone from the tuning to Milankovitch cycles could be off if they were not corroborated by radiometric dating.

4.2. Time scale for nodule growth

With a known period for the growth cyclicities of Nodule #2392, its age can be extended to the base of the outermost coating where no $^{230}Th_{ex}/^{232}Th$ data are available. The coating consists of six laminae bands (Fig. 1). With each laminae band corresponding to a short eccentricity period (95 ka), it can be inferred that the outermost coating began to grow roughly 570 ka BP (Table 6). The net growth rates for individual laminae bands can also be determined to be in the range of $3.4 \sim 6.3$ mm/Ma with an average of 4.2–4.8 mm/Ma (Table 6). This means that different laminae bands, or a specific laminae band in a different part of the nodule, might have different net growth rates, but the corresponding period would be the same.

Several investigators have presented strong evidence that the smooth-type Pacific ferromanganese nodule may be constructed by numerous microfossils whose filaments are about 2–4 nm in diameter [4–6]. Considering this circumstance, it is interesting to speculate that such microbes may reproduce roughly once every 0.5–1 year corresponding to a growth rate of around 4.6 mm/Ma. Although generation times of deep-sea microbes are largely unknown, it seems that this growth rate can match the generation time of microbes within the time scales that are typical for the Earth's surface, e.g., seasons or years or generations.

Table 6
The growth rates of the respective laminae bands in the outermost coating of Nodule #2392 and their cumulative ages according to tuning to orbital cycles and $^{230}Th_{ex}/^{232}Th$ dating, respectively

Laminae band no.	Thickness of laminae band (μm)	Cumulative age according to tuning to orbital cycles (ka)	Net growth rate according to tuning to orbital cycles (mm/Ma)	Cumulative age according to $^{230}Th_{ex}/^{232}Th$ dating (ka)
Band VI	350–418	95	3.7–4.4	76–91
Band V	428–450	190	4.5–5.3	169–198
Band IV	324–361	285	3.4–3.8	239–276
Band III	362–403	380	3.8–4.2	
Band II	562–600	475	5.9–6.3	
Band I	380–440	570	4.0–4.6	

4.3. The possible mechanism for the rhythmic growth of ferromanganese nodules

It is well established that the Earth's orbital parameters (Milankovitch cycles) have influenced the climate over the past 800 ka, and well-dated orbital rhythms in marine sediments persist at least into the mid-Oligocene (26–27 Ma) [25,26]. This climatic forcing has been recorded in many properties of marine sediments, properties as diverse as the oxygen isotopic ratios in microfossils, weight percent calcium carbonate, and sediment color [25–27], so it is reasonable that the growth of deep-sea ferromanganese nodules also should contain an Earth's orbital imprint. The mechanism causing the rhythmic growth of ferromanganese nodule is poorly understood, but it is interesting to speculate how that signal is transferred to the deep-sea environment.

The formation of Pacific deep-sea ferromanganese nodules is associated with the development of oxygen-rich Antarctic bottom water (AABW) [7,22]. Changes in bottom current oxygen, velocity, metal fluxes, particle settling and activity of microorganisms have been documented from their stromatolithic growth patterns as well as the distribution of Si, Al, Fe and Mn time series. Fig. 2 shows that the high-resolution elemental profiles exhibit numerous fluctuations during the different climatic stages. Si spikes which coincide with spikes of Al indicate they are derived from detrital particles. These spikes mostly occur during interglacial stages, e.g., Stages 3, 5, 7, 9, 11, while in glacial stages Al is usually low but the background of Si is high, with some Si spikes non-correlated with Al, for example in Stages 4, 6, 8, 14 (Fig. 2a). Exceptions occur in Stages 10 and 12 where there are peaks of Al coupled with Si. Fig. 2b reveals that Mn content tends to be generally higher, while Fe tends to be lower during glacial stages than during interglacial stages; Stages 6 and 14 are exceptions where the contents of Mn and Fe are close to each other.

The element Al, where correlated with Si, can be used as an indicator for detrital sedimentation; Si when not correlated with Al can be taken as biogenic and can be used as a proxy for biological productivity. The detrital component provides considerable paleoceanographic and paleoclimatic information. It commonly reflects either river run-off or a supply of eolian dust, along with being associated with the intensity of the bottom water flow [7]. Therefore, the peaks of Al coupled with Si in the interglacial Stages 3, 5, 7, 9, 11 might be associated with the increased aridity in the eolian source region, while in Stages 10 and 12 the peaks of Al coupled with Si are probably caused by increased erosion through intensification of bottom water flow. Variations in the Fe and Mn correlate with the intensity of biological productivity, bottom current conditions and climate [7,22,28]. The source for Fe in ferromanganese nodules is mainly considered to come from the dissolution of siliceous and calcareous plankton, therefore the supply of Fe may in part be associated with the CCD (carbonate compensation depth), which is controlled by productivity and the circulation of AABW [15,28]. Mn can be used as indicator of the redox condition; Mn in relation to Fe can be used as indication for the redox condition or more simply for oxygenation because Mn is more readily mobilized than Fe at the same redox potential [7,28]. The redox condition at the Pacific sea-floor is influenced by two factors: (1) High oxygen consumption which results in a shallower oxygen minimum zone (OMZ) in the area of high biological productivity as well as during stages of generally high productivity [31]. (2) The velocity and intensity of AABW may also influence oxygen at depth by supplying oxygenated water. Consequently, the content of Mn recorded in ferromanganese nodules may reflect the interaction of productivity and intensity of the AABW.

Fig. 2 reveals that during interglacial stages there is a greater input of detrital particles, and during glacial stages the productivity is higher and the AABW is stronger. This would result in high Mn/Fe ratios, high biogenic Si contents, and sometimes high detrital inputs caused by increased erosion (e.g., Stages 10, 12). In glacial Stages 6 and 14 the Mn/Fe ratio is close to 1, whereas in the other glacial stages it is higher. This is probably caused by a different influence of productivity and of AABW during these two glacial stages; e.g., probably with a greater influ-

ence of productivity. The content of biogenic Si also shows that the productivity is high during glacial Stages 6 and 14. Therefore, the growth of ferromanganese nodules records the variation in bottom current intensity, productivity, and detrital particle input. The Milankovitch cycles recorded by Al, Fe, Mn and Fe/Mn time series in the nodule indicate that these factors are associated with global climate change forced by orbital cycles (Fig. 5, Table 5). As the high-frequency fluctuations show (Fig. 2), however, there is much more detailed climatic information contained in the nodule's record than just glacial/interglacial variations. This is convincingly shown by the almost perfect agreement between substage boundaries and fluctuations in the elemental profiles.

The mechanism for transferring the signature may be that the changes in the Earth's motion cause alteration of the Sun's insolation and global climate changes, so that periodic changes of AABW may be induced. This in turn would cause periodic changes in oxygen content, particle and organic material fluxes, and the growth habitat of microbes. Orbital cycles may also cause fluctuations in salinity and nutrient availability, as well as upwelling, to produce changes in productivity. Growth of microbes, metal precipitation and trapping of inorganic and biogenic sedimentary particles act simultaneously, resulting in a complex stromatolithic structure of the deep-sea ferromanganese nodules driven by environmental changes. The prominent long cycles in manganese nodule growth may be mainly related to the physical-chemical condition of the environment and mass fluxes, while the short ones are probably related to the growth and propagation of microbes. The superposition of these cycles forms the cyclical alternation of laminae in manganese nodules.

5. Conclusions

Deep-sea ferromanganese nodules show four orders of basic cyclic growth pattern, namely laminae bands, laminae zones, laminae groups and laminae pairs. Power spectral analyses of its ele-mental series of Mn, Fe, Al and Fe/Mn show that they not only display conspicuous cyclicity but also bear strong resemblance to Milankovitch orbital cycles. The principal cycles in the geochemical series can be tuned to obliquity and precession, and the growth cycles of laminae bands, zones and groups correspond to the periods of eccentricity, obliquity and precession, respectively. The implied net growth rate of the nodule investigated here is 4.5 mm/Ma which is close to the growth rates of 4.6 mm/Ma determined by $^{230}Th_{ex}/^{232}Th$. This strongly supports the hypothesis that the growth of the nodule records Milankovitch orbital signatures. It is suggested that the rhythmic growth of deep-sea ferromanganese nodules is in response to global climate change forced by periodic variation of the Earth's orbital parameters. Laminae bands or laminae zones may therefore offer a new high-resolution tool to estimate growth rates of ferromanganese nodules. The successful application of Milankovitch cycle theory to the nodules suggests that it is a promising method for determining the effective growth rates of nodules as well as crusts at high time resolution when supported by precise chronological constraints such as radiochemical data. Moreover, the almost perfect agreement between substage boundaries and fluctuations in the elemental profiles suggests a great potential for the high-resolution reconstruction of past climates.

forschungsbereich 574 'Volatiles and fluids in subduction zones' at Kiel University.*[BOYLE]*

References

[1] R.K. Sorem, R.H. Fewkes, Internal characteristics of marine manganese nodules, In: G.P. Glasby (Ed.), Marine Manganese Deposits, Elsevier Oceaography Series vol. 15, 1977, pp. 147–183.

[2] J. Dymond, M. Lyle, B. Finney, D.Z. Piper, K. Murphy, R. Conard, N. Pisias, Ferromanganese nodules from MANOP sites H, S, and R-control of mineralogical and chemical composition by multiple accretionary processes, Geochim. Cosmochim. Acta 48 (1984) 931–950.

[3] P. Halbach, D. Puteanus, Morphology and composition of manganese nodules, In: P. Halbach, G. Friedrich, U. von Stackelberg (Eds.), The Manganese Nodule Belt of the Pacific Ocean: Geological Environment, Nodule Formation, and Mining Aspects, Enke Verlag, Stuttgart, 1988, pp. 17–69.

[4] C. Lin, F. Zhang, L. Bian, J. Chen, H. Shen, X. Han, Ultra-microfossils in manganese stromatolites from the east Pacific Ocean, Proc. 30th Int. Geol. Congr. 123 (1997) 182–192.

[5] F. Zhang, C. Lin, L. Bian, J. Chen, H. Shen, X. Han, The discovery of chain-like ultra-microfossils in the manganese nodules from the Pacific Ocean, J. Trace Microprobe Tech. 15 (1997) 471–476.

[6] X. Han, H. Shen, J. Chen, F. Zhang, C. Lin, L. Bian, Biogenesis and Binary mineralization of organism and chemism of polymetallic nodules from Pacific Ocean, Sci. China (D) 40 (1997) 656–661.

[7] J.R. Hein, W.A. Bohrson, M.S. Schulz, M. Noble, D.A. Clague, Variation in the fine scale composition of a Central Pacific ferromanganese crust: paleoceanographic implications, Paleoceanography 7 (1992) 63–77.

[8] V.K. Banakar, J.R. Hein, Growth response of a deepwater ferromanganese crust to evolution of the Neogene Indian Ocean, Mar. Geol. 162 (2000) 529–540.

[9] C.R. Jones, Periodicities in stromatolite lamination from the Early Proterozoic Hearne Formation, Great Slave Lake, Canada, Palaeontology 24 (1981) 231–250.

[10] J.P. Vanyo, S.M. Awramik, Stromatolites and earth–sun–moon dynamics, Precambrian Res. 25 (1985) 121–142.

[11] R. Cao, Origin and order of cyclic growth patterns in mat-ministromatolite bioherms from the Proterozoic Wumishan formation, North China, Precambrian Res. 52 (1991) 167–178.

[12] T.L. Ku, Rates of accretion, in: G.P. Glasby (Ed.), Marine Manganese Deposits, Elsevier, Amsterdam, 1977, pp. 249–267.

[13] C.A. Huh, T.L. Ku, Radiochemical observations on manganese nodules from three sedimentary environments in the North Pacific, Geochim. Cosmochim. Acta 48 (1984) 951–963.

[14] M. Segl, A. Mangini, G. Bonani, H.J. Hofmann, E. Morenzoni, M. Nessi, M. Suter, W. Wolfli, [10]Be dating of the inner structure of Mn-encrustations applying the Zurich tandem accelerator, Nucl. Instr. Methods Phys. Res. B5 (1984) 359–364.

[15] A. Eisenhauer, K. Gögen, E. Pernicka, A. Mangini, Climatic influences on the growth rates of Mn crusts during the late Quaternary, Earth Planet. Sci. Lett. 109 (1992) 25–36.

[16] F. Chabaux, A.S. Cohen, R.K. O'Nions, J.R. Hein, ^{238}U–^{234}U–^{230}Th chronometry of Fe–Mn crusts: Growth processes and recovery of thorium isotope ratios of seawater, Geochim. Cosmochim. Acta 59 (1995) 633–638.

[17] F. Chabaux, R.K. O'Nions, A.S. Cohen, J.R. Hein, ^{238}U–^{234}U–^{230}Th disequilibrium in hydrogenous oceanic Fe–Mn crusts: Palaeoceanographic record or diagenetic alteration?, Geochim. Cosmochim. Acta 61 (1997) 3619–3632.

[18] X. Han, The Rhythmic Growth of Pelagic Manganese Nodules and Its Response to Global Climate Changes, Ph.D. dissertation, Zhejiang University, 2001, pp. 14–80.

[19] S. Chen, J. Ma, The Analyzing Methods of Marine Data Processing and Their Applications (in Chinese), China Ocean Press, Beijing, 1991, pp. 481–579.

[20] X. Han, H. Wang, Y. Fang, X. Jin, S. Yang, The spectral analyses of rhythmic laminae of stromatolite in manganese nodules from Pacific Ocean and their significance, Oceanogr. China 14 (2002) 67–73.

[21] P. Halbach, M. Özkara, J. Hense, The influence of metal content on the physical and mineralogical properties of pelagic manganese nodules, Miner. Depos. 10 (1975) 397–411.

[22] U. von Stackelberg, H. Beiersdorf, The formation of manganese nodules between the Clarion and Clipperton Fracture zones southeast of Hawaii, Mar. Geol. 98 (1991) 411–423.

[23] A. Knoop, R.M. Owen, C.L. Morgan, Regional variability in ferromanganese nodule composition: northeastern tropical Pacific Ocean, Mar. Geol. 147 (1998) 1–12.

[24] F.M. Henderson, K.W. Burton, Using (^{234}U/^{238}U) to assess diffusion rates of isotope traces in ferromanganese crusts, Earth Planet. Sci. Lett. 109 (1999) 25–36.

[25] A. Berger, Milankovitch theory and climate, Rev. Geophys. 26 (1988) 624–657.

[26] A. Berger, M.F. Loutre, Pre-Quaternary Milankovitch frequencies, Nature 342 (1989) 133.

[27] J. Imbrie, J.D. Hays, D.G. Martinson, A. McIntyre, A.C. Mix, J.J. Morley, N.G. Piasias, W.L. Prell, N.J. Shackleton, The orbital theory of Pleistocene climate: support from a revised chronology of the marine δ^{18}O record, in: A. Berger et al. (Eds.), Milankovitch and Climate, Reidel, Hingham, MA, 1984, pp. 269–305.

[28] B. Finney, M. Lyle, Sedimentation at MANOP site H (eastern equatorial Pacific) over the past 400,000 years: Climatically induced redox variations and their effects on transition metal cycling, Paleoceanography 3 (1988) 169–189.

[29] D. Martinson, N. Pisias, J. Imbrie, T. Moore, N. Shackle-

ton, Age dating and the orbital theory of the ice ages development of a high-resolution 0 to 300,000-year chronostratigraphy, Quat. Res. 27 (1987) 1–29.

[30] W. Prell, J. Imbrie, D. Martinson, N. Pisias, N. Shackleton, H. Streeter, Graphic correlation of oxygen isotope stratigraphy application to the Late Quaternary, Paleoceanography 1 (1986) 137–162.

[31] T.F. Pedersen, M. Pickering, J.S. Vogel, J.N. Southon, D.E. Nelson, The response of benthic foraminifera to productivity cycles in the eastern equatorial Pacific: Faunal and geochemical constraints on glacial bottom water oxygen levels, Paleoceanography 3 (1988) 157–168.